Development of a Tabletop Setup for the Transient Current Technique Using Two-Photon Absorption in Silicon Particle Detectors

Moritz Wiehe, Marcos Fernández García, Michael Moll, Raúl Montero, F. R. Palomo, Ivan Vila, Héctor Muñoz-Marco, Viorel Otgon, and Pere Pérez-Millán

***Abstract*— The transient current technique (TCT) is widely used in the field of silicon particle detector development. So far, only laser wavelengths with a photon energy larger than or similar to the silicon bandgap (single photon absorption) were used. Recently, measurements using two-photon absorption (TPA) for silicon detector testing have been carried out for the first time. Excess carriers are only created at the focal point of the laser beam and thus resolution in all three spatial directions could be achieved. The resolution perpendicular to the incident laser beam could be increased roughly by a factor of 10. First measurements using this new method were performed at the Singular Laser Facility of Universidad del País Vasco (UPV)/Euskal Herriko Unibertzitatea (EHU). Following the initial success of the method, a compact TPA-TCT setup is under development. A first description of the setup and laser system is presented in this article.**

***Index Terms*— Femtosecond laser, radiation hardness, silicon detector, transient current technique, two-photon absorption.**

I. Introduction

THE transient current technique (TCT) has been established as a standard tool for the characterization of unirradiated and irradiated silicon particle detectors [1], [2]. In laser-TCT, laser light in the visible or near-infrared range is used to generate electron hole pairs inside the detector material. The drift current, resulting from the movement of the generated charge carriers in the biased silicon detector, is measured. The light can be injected from the top or bottom of the device under test (DUT), as well as from the edge (edge-TCT [3]). The wavelength of the light can be tuned such that charge is created only in a localized volume at the surface of the detector (visible light, e.g., 660 nm wavelength) or along the laser beam throughout the bulk of the device [near-infrared, near-infrared response (NIR), e.g., 1064 nm wavelength]. In any case, conventional TCT, based on single-photon absorption (SPA), results in a 2-D spatial resolution, since the measurement is insensitive to a change of the position of the DUT along the beam axis. To achieve a fully 3-D characterization of silicon detectors, nonlinear absorption of light can be used. The first description of two-photon absorption (TPA) can be found in [4]. The first experimental confirmation of the process [5], [6] was only possible, after the invention of the laser. TPA has a large variety of applications in many research fields and has already been used to simulate single-event upsets in electronic devices (see, e.g. [7], [8]). For silicon detector testing, a wavelength of the light is chosen such that linear absorption is negligible. In this case, a single photon does not have enough energy to create an electron hole pair and the detector is transparent for the injected light. Only with a high enough intensity at the focal point of the laser, charge carriers can be created by the absorption of two photons. The focal point of the laser can be moved inside the silicon detector resulting in a 3-D resolution. In addition, due to the use of strong focusing optics, the beamwidth is significantly smaller than in current conventional TCT setups, resulting in an improved spatial resolution transverse to the beam propagation direction. This development is especially important, following the trend of ever thinner detectors, detectors with implemented read-out circuitry (CMOS), and smaller read-out electrodes and interpixel isolation structures. TPA-TCT measurements at the Universidad del País Vasco (UPV)/Euskal Herriko Unibertzitatea (EHU) laser facility [9] have shown the potential of this new method [10]–[12]. TPA-TCT will prove useful in in-depth silicon sensor characterization and will complement the existing and well-established techniques (TCT, edge-TCT). The first compact TPA-TCT setup, using a tabletop femtosecond laser source, is under development at the Solid State Detector Laboratory at CERN and is presented in this article.

Manuscript received September 21, 2020; revised November 13, 2020; accepted December 10, 2020. Date of publication December 14, 2020; date of current version February 16, 2021. This work was supported in part by the Spanish Ministry of Economy and Competitiveness (MINECO) under Grant FPA2013-48387-C6-1-P and in part by the Wolfgang Gentner Programme of the German Federal Ministry of Education and Research under Grant 05E15CHA.

Moritz Wiehe is with CERN, 1211 Geneva, Switzerland, and also with the Physikalisches Institut, Albert-Ludwigs-Universität Freiburg, 79104 Freiburg, Germany (e-mail: m.wiehe@cern.ch).

Marcos Fernández García is with CERN, 1211 Geneva, Switzerland, and also with the Instituto de Física de Cantabria (CSIC-UC), 39005 Santander, Spain.

Michael Moll is with CERN, 1211 Geneva, Switzerland.

Raúl Montero is with the SGIker Laser Facility, UPV/EHU, 48940 Leioa, Spain.

F. R. Palomo is with the Escuela Técnica Superior de Ingenieros, 41092 Sevilla, Spain.

Ivan Vila is with the Instituto de Física de Cantabria (CSIC-UC), 39005 Santander, Spain.

Héctor Muñoz-Marco, Viorel Otgon, and Pere Pérez-Millán are with FYLA LASER S.L., 46980 Valencia, Spain.

Color versions of one or more figures in this article are available at https://doi.org/10.1109/TNS.2020.3044489.

Digital Object Identifier 10.1109/TNS.2020.3044489

II. Theory

In this section, the mechanism of charge generation via two-photon absorption is briefly discussed. A laser pulse

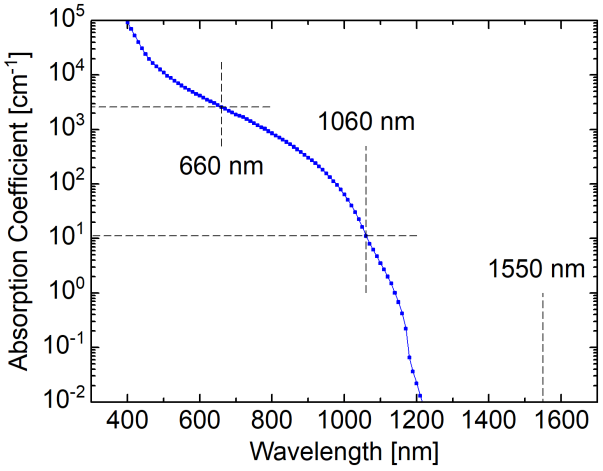

Fig. 1. Room-temperature absorption spectrum of silicon in the visible and near-infrared region. Data from [13].

propagating through a semiconductor device will be absorbed, depending on the material properties and wavelength of the laser. The changes of pulse irradiance I and phase Φ along the propagation direction z are described by

$$\frac{dI(r,z,t)}{dz} = -\alpha I(r,z,t) - \beta_2 I^2(r,z,t) - \sigma_{ex} N I(r,z,t) \tag{1}$$

$$\frac{d\Phi(r,z,t)}{dz} = \beta_1 I(r,z,t) - \gamma_1 N(r,z,t) \tag{2}$$

with r being the distance to the beam axis [8]. α and β_2 are the linear (SPA) and nonlinear (TPA) absorption coefficients, respectively. β_1 and β_2 are proportional to the real and imaginary part of the absorbing material's third-order susceptibility $\chi^{(3)}$. σ_{ex} and N are the cross section for free-carrier absorption and the number of free charge carriers. The second term in (2) describes the refraction due to free carriers.

The wavelength-dependent absorption spectrum of silicon is shown in Fig. 1. The absorption of photons with a wavelength larger than the silicon bandgap, $E_\gamma(1.1\ \mu\text{m}) = hc/\lambda \approx 1.12$ eV, is strongly suppressed. For light with longer wavelengths ($E_\gamma < 1.12$ eV), the first term in (1) can be neglected. For short pulses also, the contribution from free-carrier absorption can be neglected [14]. The remaining second term in (1) describes the two-photon absorption process we are interested in. The solution to this differential equation is

$$I(z) = \frac{I_0}{1 + \beta_2 I_0 z} \tag{3}$$

which describes the depletion of the beam due to two-photon absorption after traversing the distance z in the material with respect to the incidence irradiance I_0. The radial and time dependence was omitted here and thus (3) is not describing the change of irradiance due to a nonplanar beam. Due to the strong focusing of the laser beam to achieve two-photon absorption, the Gaussian shape of the beam dominates the spatial dependence of the irradiance and in fact beam depletion due to generating charge carriers in the small volume around the focal point can be neglected under the given experimental conditions. The irradiance of a Gaussian beam in both space and time (see, e.g. [15]) can be written as

$$I(r,z,t) = \frac{E_p}{\tau} \frac{4\sqrt{\ln 2}}{\pi^{\frac{3}{2}} w^2(z)} \exp\left[-\frac{2r^2}{w^2(z)}\right] \exp\left[-4\ln 2 \frac{t^2}{\tau^2}\right] \tag{4}$$

$$w(z) = w_0 \sqrt{1 + \left(\frac{\lambda z}{\pi w_0^2 n}\right)^2} \tag{5}$$

where τ is the full-width at half-maximum (FWHM) of the beam temporal profile. The beam radius $w(z)$ is the two-sigma radius of the beam intensity profile and is related to the FWHM of the beam by $w(z) = 2\sigma(z) = \text{FWHM}(z)/(2\ln 2)^{1/2}$. The beam radius at the waist ($z = 0$) is $w_0 \approx \lambda/\pi NA$, with the numerical aperture $NA = n \sin\theta$. n is the refractive index of the material in which the beam propagates and θ is the opening angle of the beam with respect to the beam axis. The numerical aperture is a constant and used to characterize the focusing optics. Here and in the following, λ refers to the laser wavelength in vacuum. The Rayleigh length of a Gaussian beam can be expressed as $z_0 = \pi w_0^2 n/\lambda$. At one Rayleigh length away from the focal point, the beam radius has increased to $w(z_0) = \sqrt{2} w_0$. The Rayleigh length and the beam waist define the volume in which charge carriers are produced and, for a given material, solely depend on the laser wavelength and the focusing optics. For a 1.55-μm laser pulse in silicon, using an objective with $NA = 0.5$, values of $w_0 = 1\ \mu$m and $z_0 = 6.9\ \mu$m can be achieved. The energy per pulse E_p is obtained by integrating the irradiance over time and polar coordinates

$$E_\text{p} = \int_{-\infty}^{\infty} \int_0^{2\pi} \int_0^{\infty} I(r,z,t)\, r\, dr\, d\phi\, dt. \tag{6}$$

The charge carrier density due to two-photon absorption, described by the second term of (1), is [8]

$$\frac{dn(r,z,t)}{dt} = \frac{\beta_2}{2\hbar\omega} I^2(r,z,t). \tag{7}$$

The factor of 2 in the denominator accounts for the fact that two photons need to be absorbed for one electron–hole pair. Integrating this equation over time results in the charge carrier density

$$n_{tpa}(r,z) = \frac{E_\text{p}^2 \beta_2 4\ln 2}{\tau \hbar\omega \pi^{\frac{5}{2}} w^4(z) \sqrt{\ln 4}} \exp\left[-\frac{4r^2}{w^2(z)}\right] \tag{8}$$

with $\omega = 2\pi c/\lambda$. The charge carrier density is shown as a function of the distance to the beam axis r and longitudinal distance from the focal point z in Fig. 2. The used beam parameters are shown in the figure. One can see that charge carriers are only created in close vicinity to the focal point. Since absorption is negligible at some distance from the focus, the volume in which charge is created can be moved arbitrarily inside the DUT. The spatial resolution using this method is largest in the direction perpendicular to the beam axis. Often it is desirable to measure the electric field profile as a function of depth inside the silicon bulk. To exploit the high resolution perpendicular to the beam, it is possible to inject the light from the edge of a device (edge-TCT configuration). Using TPA-TCT, this approach has the limitation that, especially for

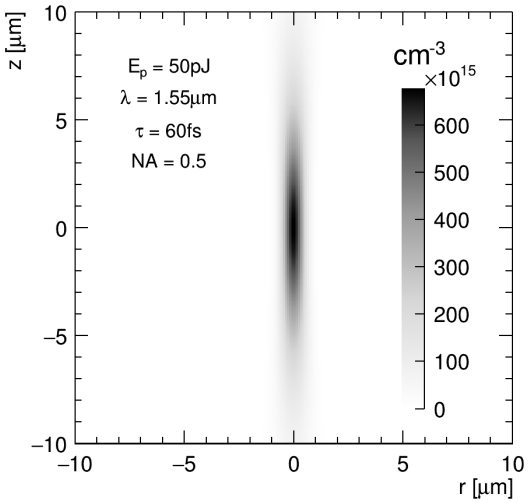

Fig. 2. Density of charge carriers created by TPA in silicon, calculated with (8). The vertical axis is parallel to the beam propagation direction with ($z = 0$) at the position of the focal point. A value of $\beta_2 = 1.5$ cm/GW [16] was used for the calculation.

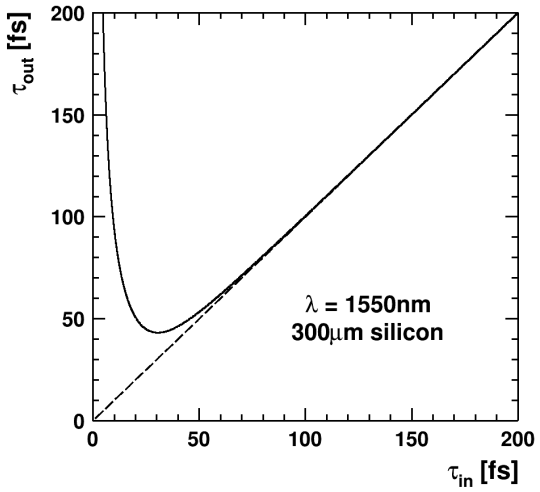

Fig. 3. Pulselength τ_{out} of a 1550-nm laser pulse after traveling through 300 μm silicon as a function of initial pulselength τ_{in}.

thin devices, the beam can be clipped at the top or bottom surfaces due to the large numerical aperture. For example, as follows from (5) for the given beam parameters, the beam diameter is as large as $2w = 87$ μm for a penetration depth of $z = 300$ μm. Since both visible and infrared light are reflected on metallic surfaces, the sensor area where the beam enters the silicon has to be free of metallic structures for SPA- and TPA-TCT. Metallic structures on the sensor surfaces, especially on the back side, can reflect the beam back into the active volume and result in artifacts in the measurement. In SPA-TCT measurements, the reflected beam will inevitably lead to additional charge carriers. In TPA-TCT, this effect, although still possible, is reduced because only focused reflections lead to unwanted absorption of light. Diffuse scattering or a divergent reflection will not lead to the creation of additional charge carriers.

The total number of created charge carriers is obtained from integrating the charge carrier density over the full volume

$$N_{tpa} = \int_V n_{tpa}(r, z)\, dV = \frac{E_{\text{p}}^2 n \beta_2 \sqrt{\ln 4}}{4\hbar c \tau \sqrt{\pi}}. \tag{9}$$

Inserting values of $E_{\text{p}} = 50$ pJ, $\tau = 60$ fs, and $\beta_2 = 1.5$ cm/GW [16] yields a value of $N_{tpa} = 11 \cdot 10^6$. In a volume of approximately $V = 4/3\pi\, w_0^2 z_0 \approx 30$ μm^3, this corresponds to an average charge carrier density of about $n_{eh} = 4 \cdot 10^{17}$ cm^{-3}.

For irradiated detectors, the SPA contribution to the signal is not negligible anymore. The ratio of the TPA signal ($\sim I^2$) to the transient SPA contribution ($\sim I$) increases linearly with the pulse irradiance. To increase the TPA/SPA ratio, it is therefore desirable to use ultrashort laser pulses. The lower limit of the pulse duration is given by dispersion, as is described in Section II-A. The total pulse energy, on the other hand, can only be increased up to an upper limit due to the threshold for plasma creation.

A. Dispersion in Silicon

The pulse temporal width is restricted by dispersion, which is very significant if the pulse is too short. In Fig. 3, the pulsewidth τ_{out} after passing through 300 μm of silicon is shown as a function of the initial pulsewidth τ_{in}. τ_{in} and τ_{out} are the FWHM of the pulse temporal profile. Dispersion effects are negligible for initial pulses longer than 60 fs but lead to a significant elongation of the pulses at shorter initial pulsewidths. The reason for this is that shorter pulses have a larger bandwidth and are therefore more affected by dispersion. The effect of dispersion on the pulsewidth can be calculated with [17]

$$\tau_{\text{out}} = \tau_{\text{in}} \sqrt{1 + \frac{16(\ln 2)^2 \text{GDD}^2}{\tau_{\text{in}}^4}} \tag{10}$$

where GDD is the group delay dispersion, which is calculated for a material with thickness L according to $\text{GDD} = \text{GVD} \cdot L$. The group velocity dispersion (GVD) can be calculated with

$$\text{GVD} = \frac{\lambda^3}{2\pi c^2} \left(\frac{\partial^2 n}{\partial \lambda^2} \right) \tag{11}$$

where the value for $\partial^2\, n/\partial\lambda^2$ can be obtained using the Sellmeier equation

$$n(\lambda) = \sqrt{1 + \sum_{i=1}^{3} \frac{A_i \lambda^2}{\lambda^2 - B_i^2}}. \tag{12}$$

The parameters A_i and B_i for silicon at room temperature, taken from [18], result in a value of $\text{GVD} = 1119.4$ fs^2/mm for a wavelength of 1.55 μm.

B. Elongation of a Laser Beam in Silicon

The position of the crossing point of two light rays, which enter a medium at a certain angle, depends on the refractive index of the medium. As a consequence, a laser beam will appear to be elongated if traveling through a medium with a higher refractive index. The Rayleigh length z_0 of the beam

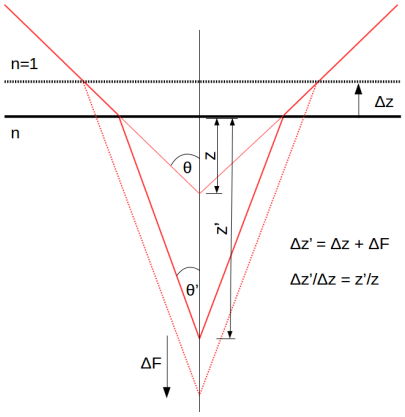

Fig. 4. Elongation of a laser beam, when entering from air into a material with a refractive index n. A movement of the sensor surface by Δz results in a shift of the focal point in the opposite direction leading to a total displacement of $\Delta z'$.

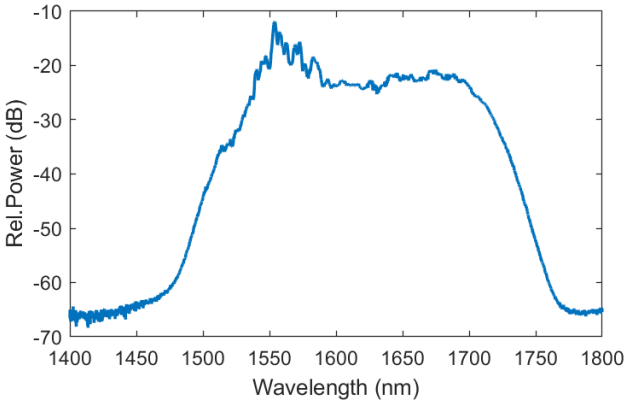

Fig. 5. Optical spectrum measured with OSA YOKOGAMA AQ-6375 (1200–2400 nm) at collimated output, 2 nm resolution, LFC1500X Factory Acceptance Test [20].

spot is different in silicon and air. Following from Snell's law and the definition of the numerical aperture of a microscope objective $NA = n \sin\theta$, the distance from the surface of the material with refractive index n to the focal point z' of a focused laser beam inside the material is

$$z' = z\sqrt{\frac{n^2 - NA^2}{1 - NA^2}} \tag{13}$$

where z is the respective distance for $n = 1$. An equivalent term can be derived directly from Snell's law and the relation of the opening angle, the beam radius, and Rayleigh-length $\tan\theta' = w_0/z_0$, with $z_0 = \pi n w_0^2/\lambda$:

$$z' = z\sqrt{\frac{z_0 \pi n^3}{z_0 \pi n - \lambda n^2 + \lambda}} \tag{14}$$

where z_0 is the Rayleigh length in silicon. The meaning of variables z and z' is depicted in Fig. 4. It is also important to realize that the position of the focal point in the laboratory frame changes, if the surface of the silicon sensor is moved. A movement of the silicon surface in the direction of the beam by Δz results in a movement of the focal point by ΔF in the opposite direction, so that the distance of the sensor surface to the focal point changes by $\Delta z' = \Delta z + \Delta F$. Either way, the scaling factor is identical so that $\Delta z'/\Delta z = z'/z$. For example, for silicon at room temperature ($n = 3.4757$ for $T = 293$ K [19]), $\lambda = 1.55$ μm and a microscope objective with $NA = 0.5$ the elongation factor is $z'/z = 3.97$. For focusing optics with smaller numerical aperture, the scaling factor converges to the material's refractive index. In TPA-TCT measurements, the position of the focal point inside the silicon sensor is important and the elongation factor has to be taken into account.

III. Experimental Setup

A. Laser System

The most important difference to a conventional TCT setup is the laser source. In TCT setups, based on SPA, usually laser wavelengths in the visible spectrum or near-infrared are used. To exploit the process of TPA, a laser with a photon energy significantly below the bandgap energy in silicon has to be used. For the setup described here, a wavelength of 1550 nm was chosen. The laser LFC1500X was custom developed by the company Fyla [20] to meet the requirements for TPA-TCT. LFC1500X is a laser system that allows for full pulse control and measurement. The system is contained in three different modules: The laser module, pulse management module, and a pulse compressor. The laser module contains the oscillator, amplifiers, and a pulse picker. The pulse frequency can be changed from about 6.8 MHz down to single shot. A TTL trigger output is obtained directly from the photo-detected signal of the laser oscillator and can be used to acquire information about the frequency in real time. From the laser module, the pulse is fed into the pulse management module with an optical fiber. From here, the beam is propagating in free space. In the pulse management module, the optical output pulse energy can be adjusted from 10 nJ down to 100 pJ, using a variable neutral density filter. A direct photo-detected signal, obtained by redirecting part of the beam to an InGaAs photo sensor, can be used to relate the peak-to-peak voltage with the pulse energy. This reference signal is used to correct measurements for fluctuations in the output power of the laser on a pulse-to-pulse basis. The laser management module also contains the automatic output shutter. The laser system is controlled with a LabView software, which was integrated into a common data-acquisition software.

Figs. 5 and 6 show the optical spectrum of the laser and an intensity autocorrelation measurement, respectively. The spectrum shows a pronounced peak around 1550 nm with a central bandwidth of ~40 nm. The tails of the spectrum range from about 1500 to 1750 nm. The intensity autocorrelation trace has a width of 120 fs, which corresponds to about 85 fs laser pulsewidth, assuming a Gaussian pulse.

The laser LFC1500X, which was used for the measurements presented in this article, was a prototype, specifically designed for the application in a TPA-TCT setup. Early measurements showed an instability over time of the TPA signal, which was not reflected in the SPA reference signal and was thus difficult to correct for. The reason for the TPA instability is believed

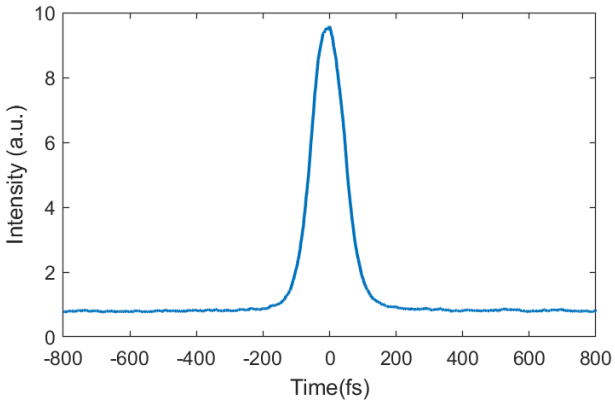

Fig. 6. Intensity autocorrelation trace at the laser output, width ~120, 10 fs resolution, LFC1500X Factory Acceptance Test [20].

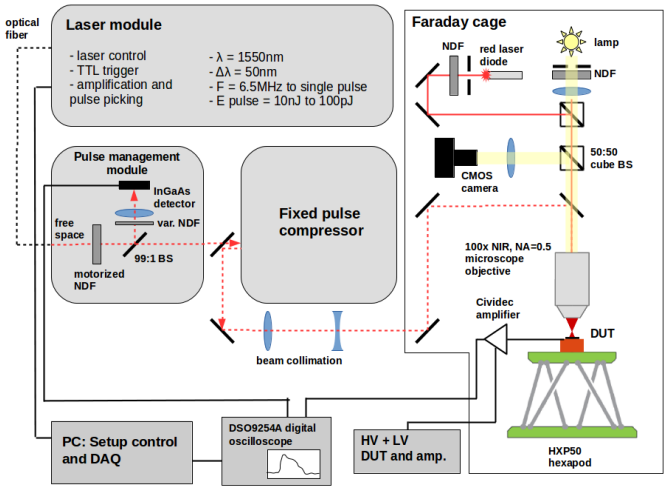

Fig. 7. Schematic view of the TPA-TCT experimental setup. The setup consists of three main parts: 1) Fyla laser system comprised of the laser module, pulse management module, and pulse compressor; 2) Faraday cage with DUT/amplifier and hexapod, focusing optics, and microscope setup; and 3) voltage supply and data acquisition.

to originate from spectral instabilities in the output of the laser, which result in fluctuations in the pulse temporal profile, thus affecting the two-photon absorption process. The laser source is under development, and technical improvements are planned to address this issue. Therefore, the pulse spectrum and temporal profile are subject to change in future versions of the laser.

B. Optical Components and Mechanics

The laser system, all optical components, and a Faraday cage, in which the DUT is placed during measurements, are mounted on a 2.5 m × 1 m Nexus passive isolation optical table. For routing the laser beam to the DUT Low GDD mirrors (Thorlabs UM10-45C) are used. The laser beam is focused onto the DUT with a 100× NIR Mitutoyo microscope objective (M Plan Apo NIR 100×, $NA = 0.5$). For precise positioning of the DUT and to perform spatial scans with high resolution, a Newport hexapod (HXP50HA-MECA) is used. A hexapod has six degrees of freedom (3× translation, 3× rotation), which can be used to ensure that the sensor has the correct orientation with respect to the laser beam. The hexapod is able to perform fine scans with a minimum incremental movement of 50–100 nm with a travel range of about 1–2 cm. The hexapod itself is mounted on a stack of two long-travel Newport linear stages to be able to easily adjust the DUT position with respect to the microscope objective prior to the start of a measurement. The linear stages are usually not moved during a running measurement. To facilitate correct DUT positioning, a custom microscope setup is installed: A CMOS camera with a white light source and a laser pointer for alignment are used to create an image, showing where the light will be injected in the DUT.

C. Sample and Data Acquisition

Two n-in-p deep diffused FZ-silicon sensors (unirradiated/irradiated) from Hamamatsu Photonics were used for the measurements presented in this article. The unirradiated sensor (FZ200P_05_DiodeL_9) has an active thickness of 209 μm. The second sensor has a thickness of about 120 μm and was irradiated with neutrons to a fluence of $1.6 \times 10^{16}\,\mathrm{n_{eq}/cm^2}$. Both sensors have an active area of $5 \times 5\ \mathrm{mm}^2$. The respective DUT is glued to a printed circuit board (PCB) which is equipped with SubMiniature version A (SMA) connectors for the bias voltage supply, read-out, and optional guard-ring connection. The glue is conductive and establishes the backside connection. The read-out electrode and guard ring on the front side of the sensor are connected to the PCB with wire bonds. A PT1000 temperature sensor is attached to the PCB close to the DUT. The DUT signal is amplified by a Cividec 2 GHz/40 dB amplifier and displayed on an Agilent Technologies DSO9254A digital oscilloscope. To monitor the power of the laser, part of the beam is directed onto a reference diode inside the laser pulse management module. Its signal is recorded with the DUT data and used in the analysis to normalize the signal to account for fluctuations in the laser output.

Fig. 7 shows a schematic view of the TPA-TCT experimental setup. All important components of the optical and data acquisition setup are shown. The pulse management module was simplified and includes only the components that are of direct relevance to the user.

IV. Measurements on an Unirradiated Detector

In this section, first measurements with the new setup are shown to demonstrate the feasibility of the method and the tabletop laser system.

A. Z-Scan

One of the benefits of TPA-TCT is the true 3-D resolution for testing silicon detectors. With conventional TCT with red, or near-infrared (<1200 nm) light, it is only possible to fully resolve the DUT by changing the illumination direction in different measurement configurations. TPA-TCT provides resolution along the beam propagation direction and thus allows for a 3-D scan of the device in a single measurement setup. Fig. 8 shows a measurement of the signal, integrated

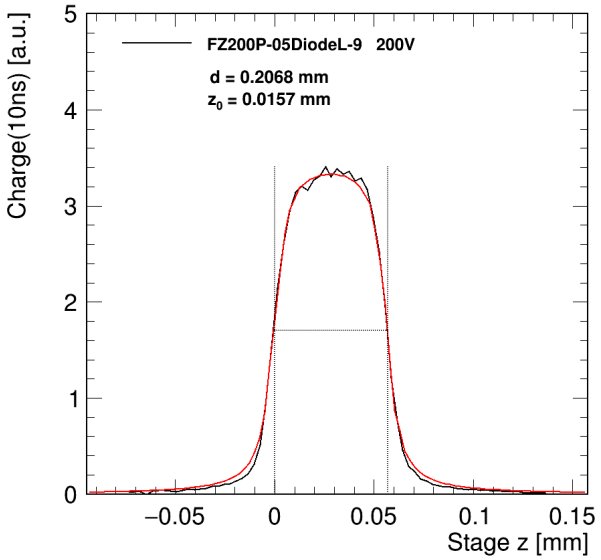

Fig. 8. Integrated signal in 10 ns as a function of z-position of the hexapod. The sensor bias voltage is constant at 200 V. The z-axis is antiparallel to the beam propagation direction.

over 10 ns, as a function of the sensor position along the beam propagation direction (z-axis). The DUT is a Hamamatsu Photonics deep diffused diode. An active thickness of 209 μm [21] was measured independently by using a capacitance–voltage scan. The zero value on the horizontal axis is arbitrarily set to the rising edge of the graph. The sensor is illuminated from the top, whereas the z-value indicates the position of the motion stage. Therefore, moving from $z = 0$ to higher values, the focal point of the laser moves from the top of the device to the backside. The width of the graph is thus a measure of the width of the depleted region of the sensor. In this case, a bias voltage of 200 V ensures that the sensor is fully depleted. For every recorded waveform, a baseline subtraction is done. Except this, no background correction is performed. The signal vanishes quickly when the focal point of the laser beam is not anymore inside the detector. This indicates that no contribution of SPA is measured. It is important to note that no resolution could be obtained in this way for conventional TCT. For a point-like charge generation at the focal point, a box function would be expected. The width of the rising and falling edges is a result of the extended volume, in which charge carriers are generated, due to the Gaussian shape of the beam. The data is fitted with a volume integral of the charge carrier distribution

$$N_{tpa}^{d}(z) = 2\pi \int_{z-d}^{z}\int_{0}^{\infty} n_{tpa}(r, z')\, r\, dr\, dz' = \frac{E_{\mathrm{p}}^2\, n\, \beta_2 \sqrt{\ln 4}}{4\, c\, \hbar\, \pi^{\frac{3}{2}}\, \tau}\left[\tan^{-1}\left(\frac{d-z}{z_0}\right) + \tan^{-1}\left(\frac{z}{z_0}\right)\right]. \quad (15)$$

The integration volume extends into infinity perpendicular to the beam and has a thickness of d in the direction of the beam. Since the charge is measured only in arbitrary units, the absolute scale of the function is absorbed by a single prefactor. An absolute measurement of the collected charge would allow to constrain the factor $E_{\mathrm{p}}^2\, \beta_2/\tau$, of which the pulse energy E_{p} and the pulse duration τ can be measured independently. The measured hexapod z-position, shown on the horizontal axis, is multiplied with the scaling factor for the effect of refraction according to (14), prior to evaluating the fit function. The fit parameters d and z_0 describe the thickness of the sensor and the Rayleigh length of the beam in silicon, respectively. The measured thickness of the device of $d = 207$ μm is close to the expected value of 209 μm, obtained from a C–V measurement. The Rayleigh length $z_0 = 15.7$ μm is larger than expected. For a numerical aperture of $NA = 0.5$, a Rayleigh length in the order of 7 μm is expected. The discrepancy is further discussed in Section IV-B.

B. Knife-Edge Scan

The knife-edge technique is a common method for measuring the profile of a laser beam. A device ("knife") is used that can be moved across the laser beam to partially block it. The intensity of the beam is measured while moving the knife across the beam. The measured intensity as a function of the knife position can then be used to calculate the beam intensity profile. The spatial resolution of the TPA-TCT setup is given by the size of the volume in which charge is generated. To measure the resolution, a knife-edge scan was carried out on a Hamamatsu Photonics deep diffused diode at a constant bias voltage of 300 V. The sensor sample features a metal cover directly on top of the active volume with a cut-out to be able to perform laser-TCT measurements. This metal cover is used as a knife edge to partially block the laser beam. While this method is easy to set up, since no additional materials are required, spatial inhomogeneities of the detector, a slight tilt of the detector with respect to the beam, and the unknown thickness of the metal cover could have negative effects on the measurement. Fig. 9 shows a measurement of the sensor signal as a function of x- and z-coordinates of the hexapod. Incremental steps of 200 nm and 1 μm were used in x- and z-direction, respectively. The z-axis of the hexapod is antiparallel to the beam propagation direction. In the right half of the figure, at $x > 1.13$ mm, the beam is blocked by the metal cover of the active area. In the top left quadrant of the figure (maximum signal), the focal point of the beam is fully inside the silicon sensor. In the bottom left quadrant, the focal point is mostly outside of (above) the sensor. Due to the strong focusing optics, the beam widens significantly when moving away from the focal point. Therefore, the resolution perpendicular to the beam direction depends on where it is measured along the beam. Away from the focal point in z-direction, the metal–silicon transition in the x-direction is less well resolved, resulting in the cone in the top half of the figure.

To obtain the beam radius $w(z)$ as a function of the distance along the beam axis z, for every hexapod position in z, the measured charge is fitted with a 2-D integral of the charge carrier distribution, replacing $r = (x^2 + y^2)^{1/2}$ in (8)

$$\int_{-\infty}^{x}\int_{-\infty}^{\infty} n_{tpa}(x', y, z)\, dy\, dx' = \frac{E_{\mathrm{p}}^2\, \beta_2 \lambda \ln 2}{4\sqrt{\ln 4}\, c\, \hbar\, \pi^{\frac{5}{2}}\, \tau\, w^2(z)}\left[1 + \mathrm{erf}\left(\frac{2x}{w(z)}\right)\right]. \quad (16)$$

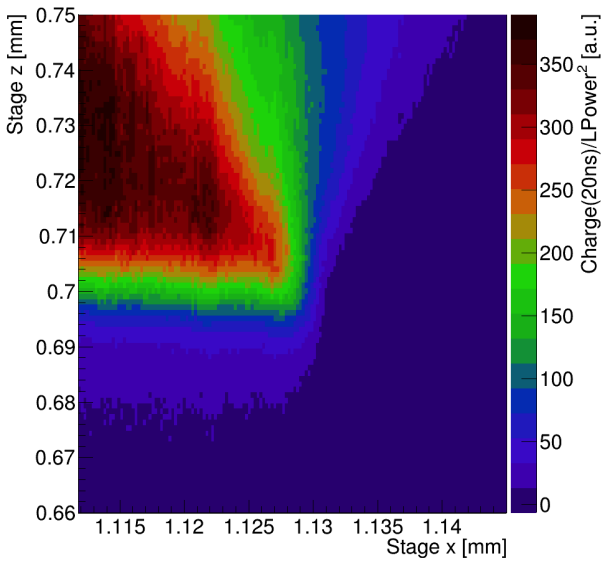

Fig. 9. Integrated signal in 20 ns as a function of x- and z-positions. The z-axis is antiparallel to the beam propagation direction.

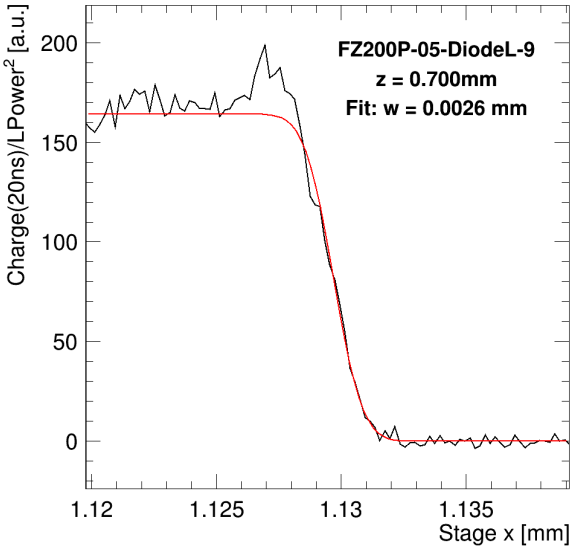

Fig. 10. Integrated signal in 20 ns as a function of the x-position of the hexapod for $z = 0.7$ mm.

The input variable x is corrected for the offset of the hexapod stage and, as before, the prefactor is absorbed in an arbitrary scaling parameter. Remaining as a fit parameter is the beam radius w. One such fit is shown as an example in Fig. 10. The obtained beam radius as a function of z is shown in Fig. 11. The figure shows the waist of the beam and the larger beam radius before and after the focal point. For low values of z, the focal point is barely inside the active volume, resulting in a low signal amplitude and therefore a slightly larger fluctuation of the obtained value of the beam radius. The beam profile is fitted with the function

$$w(z) = w_0\sqrt{1+\left(\frac{z}{z_0}\right)^2} \tag{17}$$

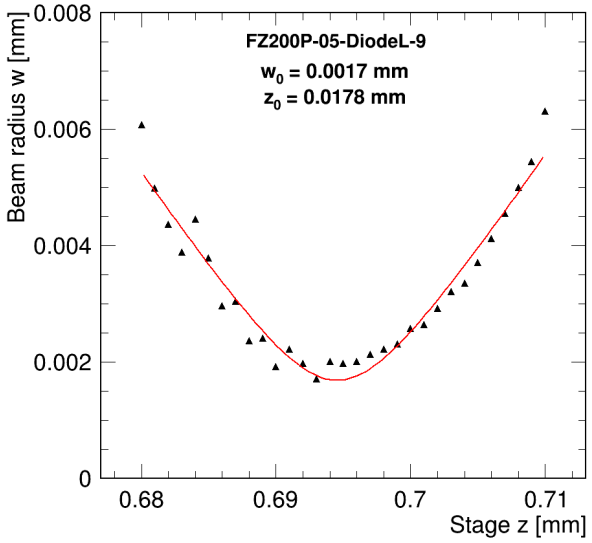

Fig. 11. Beam radius as a function of z-position of the hexapod. The data and fit are restricted to measurements around the beam waist. Obtained fit parameters w_0 and z_0 are shown.

to obtain the beam parameters z_0 and w_0. The input variable z to the fit function is corrected for the hexapod offset and multiplied by the scaling factor for correcting the effect of refraction, according to (14). The resulting beam parameters are $w_0 = 1.7$ μm and $z_0 = 17.8$ μm. These values correspond to a numerical aperture of about 0.3. The nominal numerical aperture of the focusing objective is 0.5. The discrepancy of the measured beam parameters near the focal point to the nominal numerical aperture can be a result of insufficient coupling of the beam to the objective (clipped beam, non-parallel beam) or of non-Gaussian components in the output of the laser. Further away from the focal point in the range of 0.71 mm $< z <$ 0.75 mm, which is not shown in the figure, a linear increase of the beam radius with z is observed. The slope of this linear increase indicates a value of $NA = 0.5$ which is in agreement with the expected value. The quality of the focusing depends largely on the optical setup and will be further improved.

C. Intensity Scan

The amount of charge generated by TPA depends quadratically on the beam irradiance [see (7)]. Fig. 12 shows a measurement of the integrated signal as a function of the energy per laser pulse (laser intensity). The pulse energy is varied by changing the orientation of a neutral density filter inside the laser power management module. For this measurement, the sensor was biased at 200 V. The focal point remained at a constant position in the center of the detector. The measured values are fitted with the function $Q = p_0 I^2$. The data is compatible with a purely quadratic function, indicating that no contribution from SPA can be observed. The last three data points at high intensities were excluded from the fit because for these measurements, an increase in the charge collection time was observed. The collection time should only depend on the electric field inside the device and

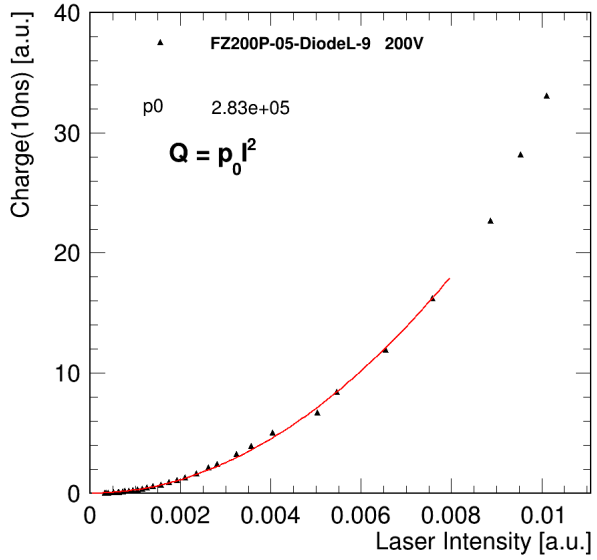

Fig. 12. Integrated signal as a function of the laser pulse energy. The energy is varied with a neutral density filter inside the laser power management module. The data was fitted with a quadratic function. Three data points at high energies were excluded from the fit due to electron–hole–plasma formation.

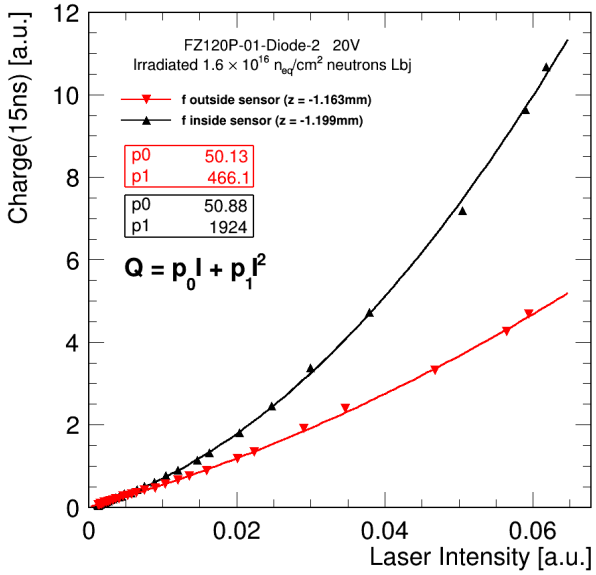

Fig. 13. Integrated signal as a function of the laser pulse energy for two different positions of the focal point. The focal point is located outside (red) and inside (black) of the sensor. Both data sets are fitted with a 2° polynomial (p0: linear term, p1: quadratic term). The sensor was irradiated with neutrons to a fluence of $1.6 \times 10^{16}\,\mathrm{n_{eq}/cm^2}$ and biased with 20 V at room temperature.

therefore stay constant. An increase in the collection time hints at the formation of an electron–hole plasma inside the sensor. This impacts the collection time and can also alter the amount of induced charge.

V. Measurements on an Irradiated Detector

A. Intensity Scan

Irradiation introduces shallow and deep-level defects in the bandgap of silicon, which lead to absorption of subband gap photons through non-TPA processes. Especially deep-level defects enhance the possibility of single-photon absorption and resonant two-photon absorption. As presented in Section IV-C, an intensity scan of an unirradiated sensor shows a purely quadratic dependence of the collected charge on the laser power and in addition no signal can be measured if the focal point is not inside the active volume of the detector although the (unfocused) beam still traverses the sensor. This changes in the case of an irradiated detector. Fig. 13 shows an intensity scan of an irradiated detector for two different positions of the focal point. The detector is an FZ-silicon sensor with a thickness of about 120 μm. The sensor was irradiated with neutrons to a fluence of $1.6 \times 10^{16}\,\mathrm{n_{eq}/cm^2}$. When this measurement was taken, the cooling system was not yet in place, and therefore, the sensor was kept at a rather low bias voltage of 20 V at room temperature. One intensity scan was performed with the focal point mostly outside of the silicon sensor (red markers) and repeated with the focal point inside the silicon (black markers). Both data sets are fitted with a second degree polynomial: $Q = p_0\ I + p_1\ I^2$. The measurement with the focal point outside the silicon results in a mostly linear curve, which is expected for defect-induced single-photon absorption. The nonzero quadratic contribution can be explained by the fact that the sensor position differs by only 30 μm to the measurement with the focal point inside the active volume. Therefore, it is assumed that part of the focal point is still inside the sensor and produces TPA. The scan at which the focal point is fully contained inside the sensor (black markers) shows a stronger quadratic dependence on the laser power because the contribution of TPA to the total signal is larger. The linear contribution is unchanged, which is also expected because the defect-induced SPA contribution is independent of the position of the focal point.

B. Z-Scan

An additional z-scan was performed on the same sample (FZ-silicon, 120 μm thickness, neutron irradiated to $1.6 \times 10^{16}\,\mathrm{n_{eq}/cm^2}$) at a constant laser power, again at a bias voltage of 20 V. Fig. 14 shows a comparison of the waveforms obtained at different positions of the focal point. The red line shows the signal when the focal point is outside the sensor and thus is produced by SPA due to irradiation-induced defects. The black line shows the signal with the focal point inside the sensor and is thus produced by the constant SPA contribution and the additional TPA at the focal point. The difference of the two signals, which is, therefore, assumed to be the TPA contribution to the overall signal, is shown as a dotted line.

Fig. 15 shows the integrated TPA signal, obtained as the difference of the total signal and the SPA contribution measured outside the active volume (red curve in Fig. 14). The horizontal axis shows the position along the z-axis of the hexapod and is thus not corrected for refraction. Lower z-values correspond to the front side of the device. When the focal point is outside of the sensor, no signal is visible due to the subtraction of the SPA contribution. Moving the sensor through the focal point, one can see that the highest TPA signal is collected near the backside of the sensor. This is expected due to the formation of a double junction in this device due to irradiation. With measuring the SPA contribution with the

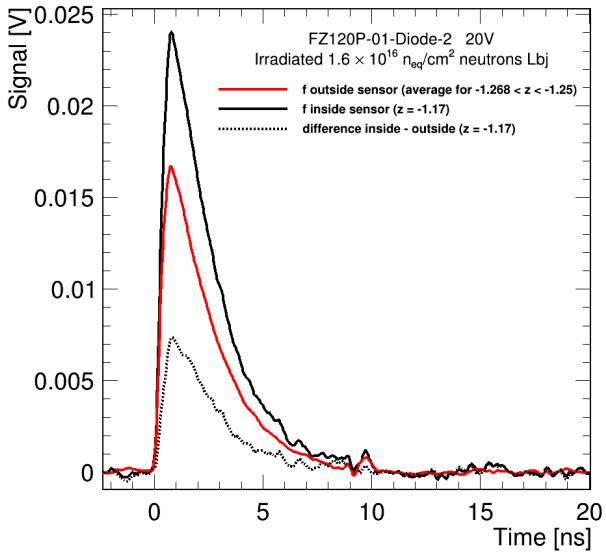

Fig. 14. Waveform for two different focal point positions and their difference. The red/black lines show the recorded waveform with the focal point outside/inside the active volume. The dotted line shows the difference of the two. When the focal point is outside of the sensor (red line), the beam still traverses the sensor. The sensor was irradiated with neutrons to 1.6×10^{16} n_{eq}/cm^2 and biased at 20 V during the measurement.

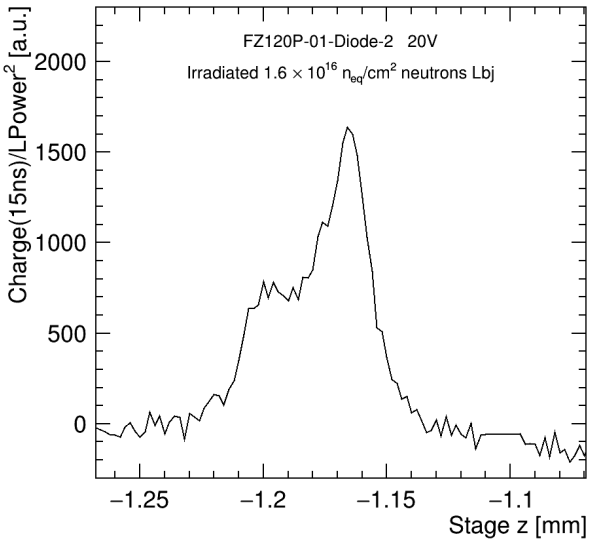

Fig. 15. Integrated TPA signal in 15 ns as a function of the z-position of the hexapod. The sensor bias voltage is constant at 20 V. The sensor was irradiated with neutrons to 1.6×10^{16} n_{eq}/cm^2. The z-axis is antiparallel to the beam propagation direction. The lower z-values correspond to the front side of the device.

focal point outside of the sensor and subtracting this signal from the total signal, when the focal point is inside the sensor, it is possible to remove the SPA offset from the data and perform TPA measurements on irradiated devices.

VI. Conclusion

TPA-TCT has proved to be a very precise characterization tool for silicon particle detectors. In the future, it will complement the existing methods for sensor characterization. In this article, the first development of a tabletop TPA-TCT setup was presented. Measurements on an unirradiated and an irradiated detector as well as a preliminary characterization of the spatial resolution of the setup were presented. First results obtained with the TPA-TCT are very promising and show that the technique is suitable to perform high-resolution measurements of unirradiated and irradiated samples. Work to improve the resolution and stability of the setup is ongoing.

Acknowledgment

The authors would like to thank Isidre Mateu for his work on the data acquisition software.

References

[1] V. Eremin, N. Strokan, E. Verbitskaya, and Z. Li, "Development of transient current and charge techniques for the measurement of effective net concentration of ionized charges (Neff) in the space charge region of p-n junction detectors," *Nucl. Instrum. Meth. Phys. Res. A, Accel. Spectrom. Detect. Assoc. Equip.*, vol. 372, no. 3, pp. 388–398, Apr. 1996.

[2] G. Kramberger, "Advanced transient current technique systems," *PoS*, vol. 227, p. 32, May 2015, doi: 10.22323/1.227.0032.

[3] G. Kramberger *et al.*, "Investigation of irradiated silicon detectors by edge-TCT," *IEEE Trans. Nucl. Sci.*, vol. 57, no. 4, pp. 2294–2302, Aug. 2010.

[4] M. Göppert-Mayer, "Über elementarakte mit zwei quantensprüngen," *Annalen der Physik*, vol. 401, no. 3, pp. 273–294, 1931.

[5] W. Kaiser and C. Garrett, "Two-photon excitation in CaF_2:Eu^{2+}," *Phys. Rev. Lett.*, vol. 7, no. 6, p. 229, 1961.

[6] D. A. Kleinman, "Laser and two-photon processes," *Phys. Rev.*, vol. 125, no. 1, p. 87, 1962.

[7] S. Buchner, "Laser simulation of single-event effects: A state of the art review," Martin Marietta Labs., Baltimore, MD, USA, Tech. Rep. ARL-CR-185, 1995.

[8] D. Mcmorrow, W. T. Lotshaw, J. S. Melinger, S. Buchner, and R. L. Pease, "Subbandgap laser-induced single event effects: Carrier generation via two-photon absorption," *IEEE Trans. Nucl. Sci.*, vol. 49, no. 6, pp. 3002–3008, Dec. 2002.

[9] UPV/EHU. *Singular Laser Facility Laboratory*. Accessed: Jan. 5, 2021. [Online]. Available: http://www.ehu.eus/en/web/sgiker/laser-tresna-aurkezpena

[10] M. F. García *et al.*, "High-resolution three-dimensional imaging of a depleted CMOS sensor using an edge transient current technique based on the two photon absorption process (TPA-eTCT)," *Nucl. Instrum. Meth. Phys. Res. A, Accel. Spectrom. Detect. Assoc. Equip.*, vol. 845, pp. 69–71, Feb. 2017.

[11] I. Vila *et al.*, "TPA-TCT: A novel transient current technique based on the two photon absorption (TPA) process," in *Proc. 25th RD Workshop*. Geneve, Switzerland: CERN, 2014, pp. 17–19.

[12] R. Palomo, I. Vila, M. Fernández, P. DeCastro, and M. Moll, "Two photon absorption and carrier generation in semiconductors," in *Proc. 25th RD Workshop*, 2014, pp. 17–19.

[13] M. A. Green, "Self-consistent optical parameters of intrinsic silicon at 300K including temperature coefficients," *Sol. Energy Mater. Sol. Cells*, vol. 92, no. 11, pp. 1305–1310, Nov. 2008. [Online]. Available: http://www.sciencedirect.com/science/article/pii/S0927024808002158

[14] E. W. Van Stryland *et al.*, "Two photon absorption, nonlinear refraction, and optical limiting in semiconductors," *Opt. Eng.*, vol. 24, no. 4, Aug. 1985, Art. no. 244613.

[15] S. Orazio, *Principles of Lasers*. New York, NY, USA: Springer, 2010.

[16] A. D. Bristow, N. Rotenberg, and H. M. van Driel, "Two-photon absorption and kerr coefficients of silicon for 850–2200nm," *Appl. Phys. Lett.*, vol. 90, no. 19, May 2007, Art. no. 191104, doi: 10.1063/1.2737359.

[17] I. Walmsley, L. Waxer, and C. Dorrer, "The role of dispersion in ultrafast optics," *Rev. Sci. Instrum.*, vol. 72, no. 1, pp. 1–29, Jan. 2001, doi: 10.1063/1.1330575.

[18] B. Tatian, "Fitting refractive-index data with the Sellmeier dispersion formula," *Appl. Opt.*, vol. 23, no. 24, pp. 4477–4485, 1984.

[19] H. H. Li, "Refractive index of silicon and germanium and its wavelength and temperature derivatives," *J. Phys. Chem. Reference Data*, vol. 9, no. 3, pp. 561–658, Jul. 1980, doi: 10.1063/1.555624.

[20] *Fyla*, Valencia, Spain, 2020. [Online]. Available: https://www.fyla.com

[21] E. C. Rivera, "Advanced silicon sensors for future collider experiments," *Sensores de silicio Avanzados Para Futuros Experimentos Colisionadores*, vol. 90, Sep. 2017, Art. no. 191104. [Online]. Available: https://cds.cern.ch/record/2291517